RSC Advances

PAPER

View Article Online
View Journal | View Issue

Cite this: *RSC Adv.*, 2017, **7**, 37765

Size-dependent optical and thermochromic properties of $Sm_3Fe_5O_{12}$

Huanhuan Liu,†[a] Long Yuan,†[ab] Hui Qi,[c] Yanyan Du,[d] Shan Wang[e] and Changmin Hou*[a]

Received 23rd May 2017
Accepted 4th July 2017

DOI: 10.1039/c7ra05803a

rsc.li/rsc-advances

Reversible thermochromic inorganic materials of $Sm_3Fe_5O_{12}$ with different particle sizes have been synthesized by a conventional high temperature solid state reaction method (2.51 μm) and sol–gel method (0.16 μm). The as-prepared samples were characterized by powder X-ray diffraction (XRD), scanning electron microscopy (SEM), infrared spectroscopy (IR), Raman, X-ray photoelectron spectroscopy (XPS) and UV-vis-NIR spectroscopy. The sizes of $Sm_3Fe_5O_{12}$ particles have a significant difference effect on the color of pigments. The absorption peak shifts to lower wavelength with the increase of particle size. The bandgap and lattice parameter increase with the decrease in particle size. Thermochromism for $Sm_3Fe_5O_{12}$ synthesized by the solid state reaction method showed a change in color from dark green to reddish brown and the samples synthesized by a sol–gel method changed from bright yellowish green to yellow. The cause of the thermochromism is the continuous red shift of ligand–metal charge transfer with the increase of temperature. This work suggests that the properties of thermochromic materials could be tuneable by particle size.

1 Introduction

Thermochromic materials have the ability to present reversible or irreversible change in color with respect to temperature stimulus, which can be used as temperature indicators temperature sensitive paint, temperature sensors, thermochromic ink, colored clothing, laser warnings, and intelligent temperature control coatings.[1,2] Organic compounds with thermochromic properties are used under 400 K because of their low thermal stability, besides, organic molecules are harmful to organisms. Inorganic thermochromic materials are regarded as potential alternatives due to their excellent thermal stability and durability over a wide temperature range. Though some inorganic compounds possess thermochromic properties, their application is restricted because of their toxicity and carcinogenicity, such as chromium compounds, mercury compounds, and other metal halides.[3] Irreversible thermochromic inorganic materials cannot be reused because of thermal decomposition or transformation, such as $Zn_3(PO_4)_2$: Mn_{2+}, $CoCO_2$, NiC_2O_4.[4,5] At present, the categories of reversible thermochromic inorganic materials are limited, mainly vanadium dioxide (VO_2) and tungsten- or molybdenum-based oxides.[6–9] Therefore, the producing nontoxic and reversible inorganic thermochromic materials are pressing. Rare-earth iron garnet $Y_3Fe_5O_{12}$ and $Sm_3Fe_5O_{12}$ are reported to possess reversible thermochromic properties.[10,11] The rare-earth iron garnet ($RE_3Fe_5O_{12}$) not only has significant thermochromic behavior, but also has excellent physical properties, which can be widely used in microwave field.[12,13] The rare-earth iron garnet ($RE_3Fe_5O_{12}$) belong to cubic crystallographic system with space group $Ia\bar{3}d$, in which unit cell contains eight $RE_3Fe_5O_{12}$ molecules and the crystal lattice contains three crystallographic sites, the tetrahedral site 24d (Fe^{2+}), the octahedral site 16a [Fe^{3+}], the dodecahedral site 24c {RE^{3+}}.[14] There is no effective close-packed structure in the garnet ferrite, which cannot be distorted to a lower symmetry and the stability of rare earth garnet ferrite decreases with the increase of the radius of rare earth ions.[15] The $RE_3Fe_5O_{12}$ with small radius of rare earth ions (Sm–Lu, and Y) can be prepared by solid state reaction,[16,17] while $RE_3Fe_5O_{12}$ with large radius of rare earth ions (Pr, Nd) only can be synthesized by mild hydrothermal method[18] or low temperature liquid phase epitaxy technique.[19]

Size-dependent physicochemical properties have been investigated in many materials in the last two decades, such as magnetic,[20,21] catalytic properties,[22–24] gas sensing properties[25] and optical properties.[26] In addition, grain size has a very significant impact on color of the sample, for example, with the increase of the grain size, the color of the CdSe nanoparticles

[a]State Key Laboratory of Inorganic Synthesis and Preparative Chemistry, College of Chemistry, Jilin University, Changchun 130012, P. R. China. E-mail: houcm@jlu.edu.cn; Fax: +86-431-85168624; Tel: +86-431-85168986

[b]State Key Laboratory of Superhard Materials, Jilin University, Changchun 130012, P. R. China

[c]The Second Hospital of Jilin University, Changchun 130041, PR China

[d]Green Chemical Engineering Technology Research Center, Shanghai Advanced Research Institute, Chinese Academy of Sciences, Shanghai 201210, PR China

[e]Department of Materials Science and Engineering, Jilin Institute of Chemical Technology, 45 Chengde Street, Jilin 132022, P. R. China

† These authors contributed equally.

was deepened.[27] Grain size govern the color of the substance originates in the variation of the bandgap and thereby give rise to absorption wavelength shift.[28,29] Size-dependent thermochromism has been found in CuO quantum dots due to the tunable electron–phonon coupling with nanocrystal size evolution.[30] However, there are few reports about the research of size-dependent thermochromism.

In previous work, we developed an *in situ* optical and structural characterization method for the studying of chemical pressure effect on thermochromic property of $Sm_{3-x}Bi_xFe_5O_{12}$.[31] In this paper, we report grain size-dependent properties of thermochromic material of $Sm_3Fe_5O_{12}$. $Sm_3Fe_5O_{12}$ with different particle size were synthesized by two synthetic methods. UV-vis absorption spectra showed that the bandgap increased with the decreasing particle size, and the color becomes lighter associated with blue shift. Reversible thermochromic between room temperature and 240 °C originates from red shift caused by a change in the ligand field around the chromophore. This indicates that the optical properties can be controlled and adjusted according to the required application by optimizing the particle size.

2 Experimental

2.1 Preparation samples

Pure $Sm_3Fe_5O_{12}$ powders were prepared by traditional solid-state reaction method and sol–gel method respectively. Solid-state reaction: the stoichiometric amounts of high purity Sm_2O_3 and Fe_2O_3 were mixed evenly by grinding in agate mortar. Then, the blend was calcined at 1200 °C for 8 h and 1400 °C for 10 h with additional grinding after 8 h. $Sm_3Fe_5O_{12}$ were prepared after cooling. Samples were grinding for a long time until the sample has a tendency to stick to the mortar (about 30 min), and particle size distribution, structure and optical spectroscopy properties were characterized after grinding. Sol–gel method: the stoichiometric amounts of $Fe(NO_3)_3\cdot 9H_2O$ and citric acid were dissolved in aqueous solution and the required amounts $Sm_3(NO_3)_3$ was dissolved in another aqueous solution. The two solutions were mixed and began to stir for three days. The ammonia was added with drop by drop to above solution to adjust the value of PH $\sim$ 7. Three days later, the solution was heated from room temperature to 85 °C at the rate of 10 °C h^{-1} to form the gel. The gel was dried at 110 °C h^{-1} for 24 h and then treated at 950 °C for 12 h after being grinded.

2.2 Characterization

Powder X-ray diffraction patterns were recorded on a Rigaku D/Max 2500V/Pc X-ray diffractometer with Cu Kα radiation (λ = 1.5418 Å) at 50 kV, 200 mA and room temperature. The step scanning was set in an angle range of $10^\circ \leq 2\theta \leq 80^\circ$ with increments of 0.02° and a scanning speed of 3° min^{-1}. Infrared spectra (IR) were performed in a range of 400–1500 cm^{-1} by Fourier transform infrared (FTIR) spectrometer. Raman spectra were characterized on Renishaw inVia Confocal Raman spectrometer with a 532 nm excited wavelength laser. The photographs of thermochromism at different temperature were obtained using camera. The CIE 1976 color parameters have been recorded by a NR200 type high-quality portable colorimeter (Shenzhen 3NH Technology Co., LTD) equipped with a standard D65 (Daylight, color temperature: 6504 K) with a 10° observer angle. Temperature-dependent ultraviolet-visible-near infrared (UV-vis-NIR) diffuse reflectance spectra were measured on Hitachi U-4100 UV-vis spectrometer equipped with temperature control accessory consists of a ceramic heating piece and temperature controlling device. Absorption coefficients (α/S) were calculated based on the reflectance by Kubelka–Munk transformation: $\alpha/S = (1-R)^2/2R$, where R is the reflectance at the given wavelength, α is the UV-vis absorption coefficient, and S is the scattering coefficient. The S value is supposed to be particle size independent since grains size is larger than a few micrometers. X-ray photoelectron spectroscopy (XPS) measurements were performed by Thermo ESCALAB250 spectrometer with a monochromatic AlK_α source.

3 Results and discussion

3.1 SEM and particle size distribution

Fig. 1 show SEM and particle size distribution graphs of the samples of $Sm_3Fe_5O_{12}$ synthesized by two different methods. It is obviously observed that the particle size of $Sm_3Fe_5O_{12}$ gained by solid state reaction is larger than that obtained by sol–gel method. The particle size were estimated using 100 distinct particles. From Fig. 1(c) it can be seen that the grain size of the samples is mainly distributed in 1.0–2.0 μm, the average grain size is 2.51 um and the maximum is about 7.2 μm. Fig. 1(d) shows the average particle size of $Sm_3Fe_5O_{12}$ samples gained by sol–gel method is 0.16 μm and the particle size is mainly distributed in 0.12–0.2 μm, the maximum is about 0.3 μm. From

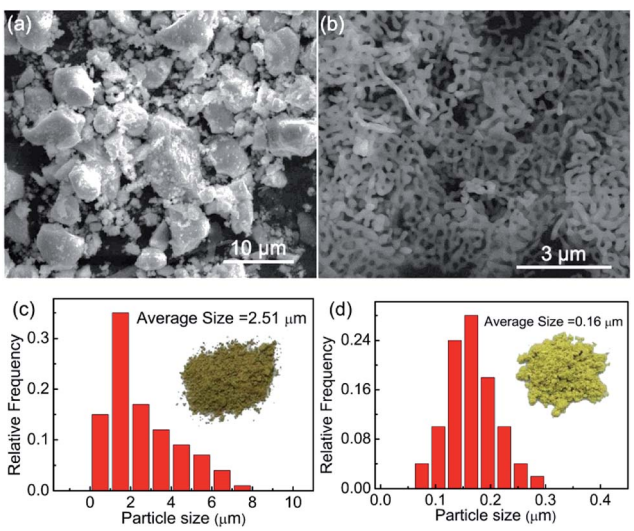

Fig. 1 (a) SEM graph of $Sm_3Fe_5O_{12}$ samples synthesized by solid state reaction method; (b) SEM graph of $Sm_3Fe_5O_{12}$ samples synthesized by sol–gel method; (c) particle size distribution of $Sm_3Fe_5O_{12}$ samples synthesized by solid state reaction method; (d) particle size distribution of $Sm_3Fe_5O_{12}$ samples synthesized by sol–gel method. The calculated number for each $Sm_3Fe_5O_{12}$ sample is 200.

the graphs it can be observed that the samples synthesized by two different methods have a significant difference in color.

3.2 Structural analysis

Fig. 2 shows the refinement results of powder XRD patterns of the samples $Sm_3Fe_5O_{12}$ with different particle size. The pattern is consistent with the standard spectrum and without any detectable impure phase. The results indicate the samples have only a single phase of the garnet structure. The refinement results show that the space groups of two samples were all $Ia\bar{3}d$. The lattice constant of $Sm_3Fe_5O_{12}$ with small particle size have increased, which is in agreement with the literatures.[32–34] The cell parameter of $Sm_3Fe_5O_{12}$ is 12.5350 Å for the large sized samples, while expands to 12.5413 Å for the smaller sized samples. HRTEM result of $Sm_3Fe_5O_{12}$ synthesized by sol–gel method was shown in Fig. 3. The measured *d*-value of the observed plane lattice is 5.29 Å. According to the power XRD results, the distance along the {211} plane is 5.12 Å, which indicates that the lattice of sol–gel method prepared $Sm_3Fe_5O_{12}$ sample is expanded.

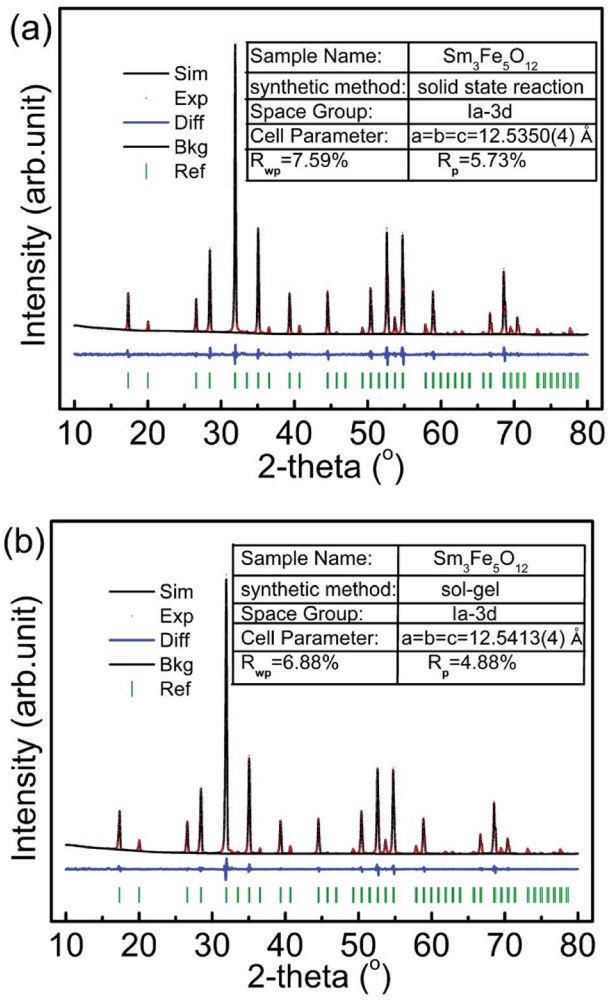

Fig. 2 Powder X-ray diffraction patterns and Rietveld refinement results of $Sm_3Fe_5O_{12}$ prepared by: (a) solid state reaction method and (b) sol–gel method.

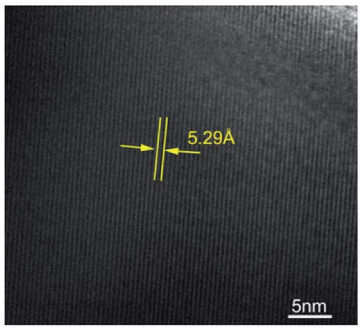

Fig. 3 HRTEM results of $Sm_3Fe_5O_{12}$ synthesized by sol–gel method.

3.3 FTIR spectra

Fig. 4 presents the FTIR spectra of $Sm_3Fe_5O_{12}$ with different particle size. From Fig. 4 it can be seen that there are three absorption peaks in the range of 500–650 cm^{-1} for each $Sm_3Fe_5O_{12}$ samples, which were the characteristic peaks of the asymmetric stretching vibration of the group Fe–O of tetrahedral.[35] It is worthwhile to note that a red shift of the main peak from 584.9 cm^{-1} to 579.2 cm^{-1} with the decrease of the particle size is associated with the dilation of the Fe–O bonds as the particle size decreases.[36] In addition, the intensity of these absorption bands is strengthened with the decrease of particle size, which is related to the surface effect.[37]

3.4 Raman microspectrometry

Fig. 5 shows the Raman microspectrometry of $Sm_3Fe_5O_{12}$ with different particle size. These two samples with different particle size show very similar spectral structure because they are isostructural. Though there are 98 vibration modes at the Brillouin zone center of rare earth iron garnet structure crystals, 55 ($5A_{1u} + 5A_{2g} + 5A_{2u} + 10E_u + 14F_{1g} + 16F_{2u}$) of them are silent and only F_{1u} is an acoustic mode. The all Raman active modes of the garnet are $3A_{1g} + 8E_g + 14F_{2g}$, corresponding to internal modes, translational and rotatory modes.[38] The distribution of all the observed Raman modes is shown in Fig. 5. The results were

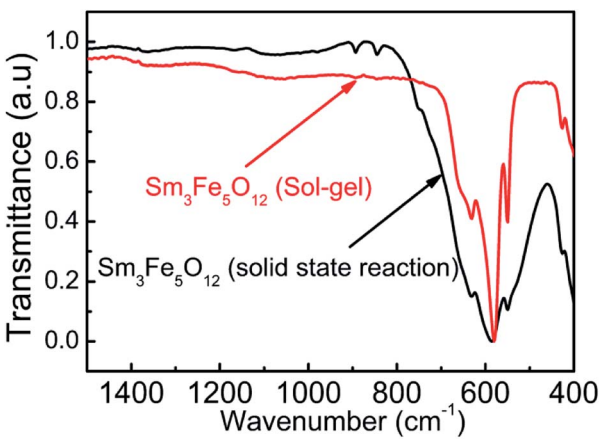

Fig. 4 The FTIR spectra of $Sm_3Fe_5O_{12}$ synthesized by two different method in the range of 400–1500 cm^{-1}.

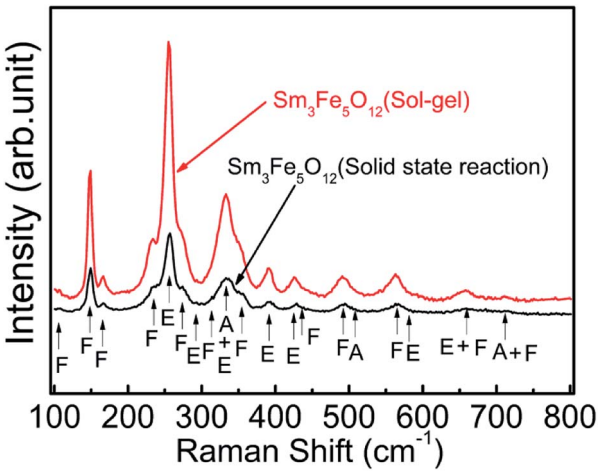

Fig. 5 Raman microspectrometry of $Sm_3Fe_5O_{12}$ synthesized by two different methods in the range of 100–800 cm^{-1} at room temperature.

consistent with the $Sm_3Fe_5O_{12}$ prepared by the hydrothermal method.[39]

3.5 XPS spectra

Chemical environment of Fe in different sized $Sm_3Fe_5O_{12}$ samples were characterized by XPS of Fe 2p detailed spectra (Fig. 6). Asymmetric doublet with distinct satellite peaks of Fe 2p orbitals are shown in both of the as-prepared two samples. Satellite peaks locate at higher binding energy than main peaks of *c.a.* 8 eV, which indicates the valence state of Fe is +3.[40] There are two crystallographic sites of Fe in $Sm_3Fe_5O_{12}$ crystal lattice, *i.e.* tetragonal and octahedral sites, which could also be discriminated from XPS spectra.[41,42] The binding energy for tetrahedral site of Fe is 723.9 and 710.5 eV for Fe $2p_{1/2}$ and Fe $2p_{3/2}$, respectively, while the binding energy for octahedral site of Fe is 727.2 and 712.7 eV for Fe $2p_{1/2}$ and Fe $2p_{3/2}$, respectively. A comparison of two materials shows that the intensity of the peak of $Sm_3Fe_5O_{12}$ synthesized by solid state reaction method is enhanced. It reveals that high temperature increases the degree of oxidation and the density of the samples. The high-density surface generates extra surface energy and promotes the oxidation reaction.[43]

3.6 Optical properties and thermochromism

Fig. 7 presents the room-temperature UV-vis-NIR diffuse reflectance and absorption (*i.e.*, Kubelka–Munk transformed reflectance) spectra of $Sm_3Fe_5O_{12}$ synthesized with different particle size in the range of 200–1200 nm. According to the optical measurements, the greenish color of $Sm_3Fe_5O_{12}$ is assigned to a ligand–metal charge transfer in violet region with Fe^{3+} d–d transitions in the orange-red region. The band at 488 nm are the ligand–metal charge transfer from 2p orbitals of O^{2-} to the empty 3d orbitals of Fe^{3+} ($O^{2-} + Fe^{3+} \rightarrow O^{-} + Fe^{2+}$), which is 485 nm for $Y_3Fe_5O_{12}$.[10] The absorption bands around 610 nm and a shoulder at 700 nm correspond to the $^6A_1 \rightarrow {}^4T_1$ transition of Fe^{3+} in octahedral site and the $^6A_1 \rightarrow {}^4T_1$, $^4T_2$

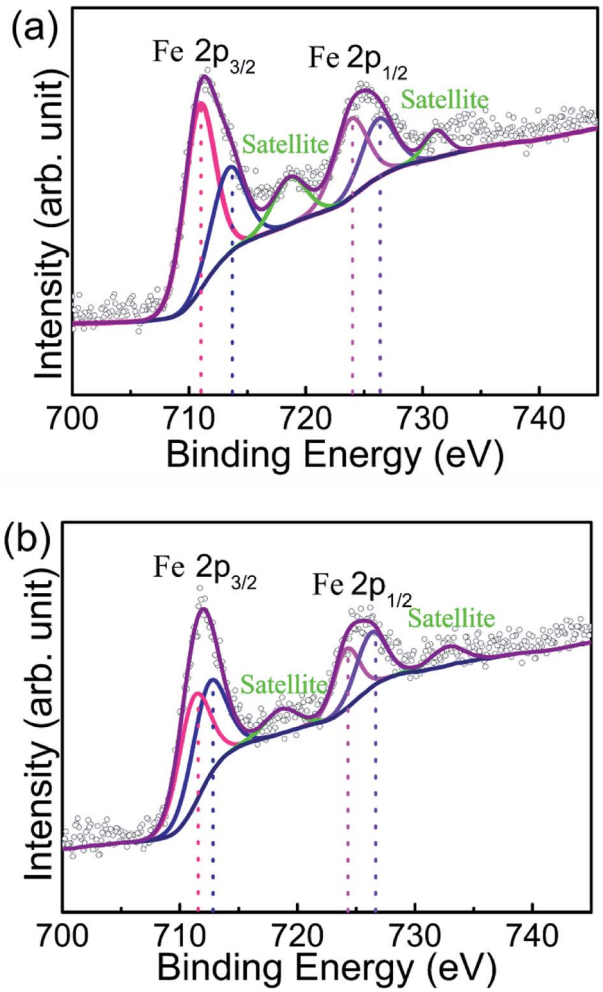

Fig. 6 XPS spectra of $SmFe_5O_{12}$ samples prepared by (a) solid state method and (b) sol–gel method, respectively. Binding energy curves of Fe $2p_{1/2}$ (pink) and Fe $2p_{3/2}$ (blue) are fits to the data (black open circles) using mixed Gaussian–Lorentzian functions, and red curves represent the sum of the peak fits. Satellite peaks are simulated with the same method marked with green lines. The Shirley method was used to subtract backgrounds.

transition of Fe^{3+} in tetrahedral site. Besides, band around 900 nm originate from the $^6A_1 \rightarrow {}^4T_1$ transition of Fe^{3+} in octahedral site. It can be seen from Fig. 7 that a blue shift (from 488 nm to 450 nm) of ligand-to-metal charge transfer with the decrease of the particle size while the position of d–d transitions is almost unchanged. The insert graphs of Fig. 7 show that the bandgap of $Sm_3Fe_5O_{12}$ with different particle size are 2.02 eV (solid state reaction method) and 2.28 eV (sol–gel method), respectively. The bandgap increases with the decrease of the particle size. The absorption intensity decreases with decreasing particle size due to enhancement of reflection strength associated with the reflection surface increase.

Fig. 8 show temperature dependent UV-vis absorption spectra and the evolution of bandgap for $Sm_3Fe_5O_{12}$ with different particle size in the temperature range of 40–240 °C. From Fig. 8 it can be seen that continuous red shift of the absorption bands at 488 nm, whereas the positioning of d–d

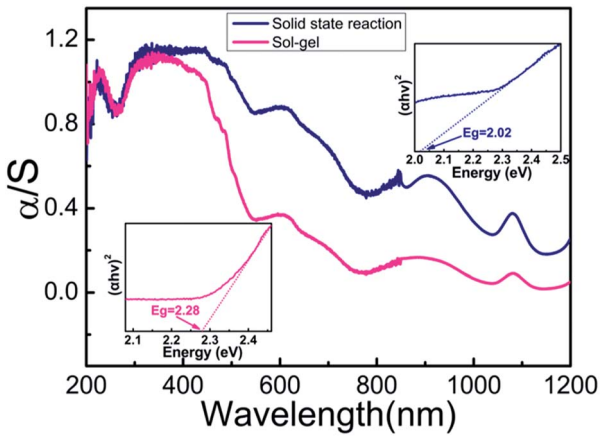

Fig. 7 Room temperature α/S spectrum (Kubelka–Munk transformation) and bandgap energy of $Sm_3Fe_5O_{12}$ synthesized by two different methods.

	$Sm_3Fe_5O_{12}$ solid state reaction method		$Sm_3Fe_5O_{12}$ sol-gel	
Temperature	CIE-Lab parameter	Photograph	CIE-Lab parameter	Photograph
40 °C	L*=36.3 a*=0.5 b*=27.2		L*=64.7 a*= -4.5 b*=48.8	
80 °C	L*=34.4 a*= -0.6 b*=24.6		L*=63.6 a*=-3 b*=47.5	
120 °C	L*=33.6 a*=0.8 b*=23.6		L*=62.5 a*= -2.2 b*=45.9	
160 °C	L*=26.5 a*=4.6 b*=21.4		L*=59 a*=1.8 b*=50.9	
200 °C	L*=26 a*=7.5 b*=23.3		L*=56.9 a*=3.7 b*=50.4	
240 °C	L*=24.8 a*=9.2 b*=22.8		L*=56.7 a*=7 b*=50.2	

Fig. 9 Photographs at different temperature and CIE-Lab parameters of $Sm_3Fe_5O_{12}$ with different particle size.

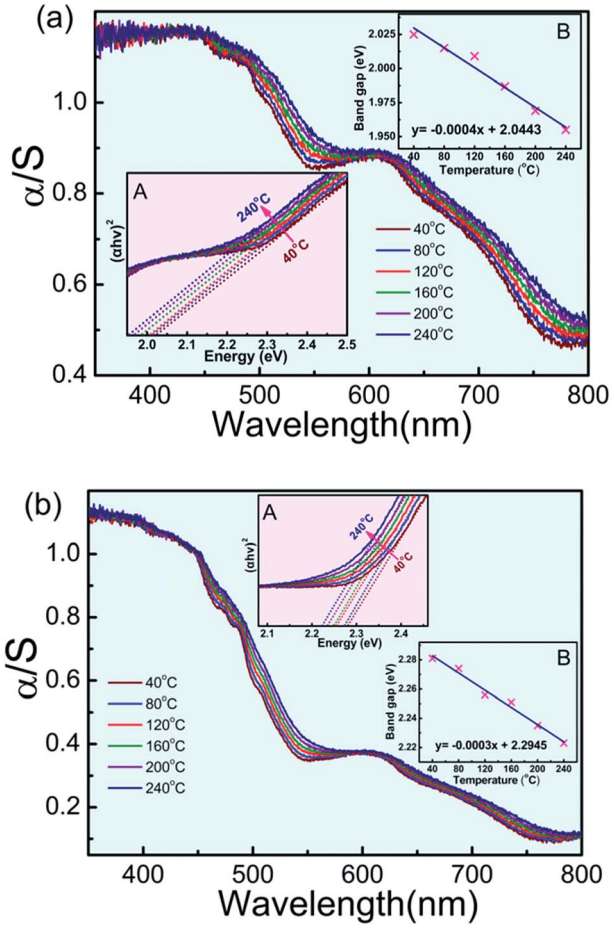

Fig. 8 Temperature dependent UV-vis spectra of $Sm_3Fe_5O_{12}$: (a) prepared by solid state method, (b) prepared by sol–gel method. Insets A and B show the Tauc plots of the UV-vis spectra and linear fitting of the energy bandgap dependent on temperature of $Sm_3Fe_5O_{12}$ synthesized by two different method.

transitions is almost unchanged. This continuous red shift is due to the slightly expansion of ionic bonds with temperature increasing according to the lattice constant increase with the increasing of temperature.[11] Unit-cell expansion causes a reduction of the electrostatic interaction of d electrons so the $O^{2-} \rightarrow Fe^{3+}$ charge transfer requires lower energy. Tauc plots of the UV-vis spectra and linear fitting of the energy bandgap dependent on temperature show bandgap energy is getting lower with increasing temperature, which means absorption peak shifts to long wavelength side as the temperature increases. This result correspond with the red-shift of UV-vis spectra.

Fig. 9 show the photographs of thermochromism and L^*ab parameters for $Sm_3Fe_5O_{12}$ with different particle size. Thermochromic behaviour of $Sm_3Fe_5O_{12}$ was investigated from 40 °C to 240 °C. From Fig. 9 the macroscopic thermochromic behaviour can be obviously observed in the range of 40–160 °C, but significant thermochromic phenomenon were not detected beyond 160 °C. The color of $Sm_3Fe_5O_{12}$ synthesized by solid state reaction method changed from blackish green to brown with the increasing of temperature, while $Sm_3Fe_5O_{12}$ synthesized by sol–gel method changed from bright yellow green to yellow. The color at room temperature of $Sm_3Fe_5O_{12}$ with different particle size originate from the combination of an $O^{2-} \rightarrow Fe^{3+}$ ligand-to-metal charge transfer at 2.54 eV (solid state method), 2.76 eV (sol–gel) and d–d transitions at 1.38 and 2.03 eV.[10] The reason for caused the colour change is continuous red shift of the absorption bands associate with the expansion of ionic bonds with temperature increasing, which is proved by the increase of the lattice parameter with temperature.[11] The electrostatic interaction of the d electrons reduced go along with the elongation of ionic bonds, which means the d^6 energy level is in a lower position and the charge transfer required lower energy.

4 Conclusions

In conclusion, we used solid state reaction method and sol–gel method to synthesize $Sm_3Fe_5O_{12}$ with different particle size,

which display a significant color difference. $Sm_3Fe_5O_{12}$ with different particle size were cubic crystallographic system with the space group of $Ia\bar{3}d$ and lattice parameter increases with the decreases of particle size. The color difference originate from the increases of the bandgap with the decrease of the particle size, which lead to the absorption band shifts to shorter wavelength side and thereby the color of $Sm_3Fe_5O_{12}$ with small particle size is brighter. The thermochromic phenomenon is attributed to the reduction of energy required for charge transfer with temperature increasing, resulting in continuous red shift of the absorption edge. The study means that the optical properties of thermochromic materials could be adjustable by optimizing the particle size.

Acknowledgements

This work was supported by the "Twelfth Five Year" Project (No. 2015-466) and "Thirteenth Five Year" Project (No. JJKH20170217KJ) of Science and Technology Research in the Education Department of Jilin Province and the Natural Science Fund of Jilin Provincial Science & Technology Department (No. 20160101326JC).

References

1 E. Lataste, A. Demourgues, J. Salmi, C. Naporea and M. Gaudon, *Dyes Pigm.*, 2011, **91**, 396–403.
2 M. Gaudon, P. Deniard, L. Voisin, G. Lacombe, F. Darnat, A. Demourgues, J.-L. Perillon and S. Jobic, *Dyes Pigm.*, 2012, **95**, 344–350.
3 J. H. Day, *Chem. Rev.*, 1968, **68**, 649–657.
4 G. Salek, A. Demourgues, V. Jubera, A. Garcia and M. Gaudon, *Opt. Mater.*, 2015, **47**, 323–327.
5 A. Seeboth and D. Lötzsch, *Thermochromic and Thermotropic Materials*, Taylor & Francis Group, 2013, ISBN-13: 978-981-4411-03-5.
6 M. M. Seyfouri and R. Binions, *Sol. Energy Mater. Sol. Cells*, 2017, **159**, 52–65.
7 R. Chen, L. Miao, H. L. Cheng, E. Nishibori, C. Y. Liu, T. Asaka, Y. Iwamoto, M. Takata and S. Tanemura, *J. Mater. Chem. A*, 2015, **3**, 3726–3738.
8 M. Gaudon, P. Deniard, A. Demourgues, A.-E. Thiry, C. Carbonera, A. Le Nestour, A. Largeteau, J.-F. Létard and S. Jobic, *Adv. Mater.*, 2007, **19**, 3517–3519.
9 L. C. Robertson, M. Gaudon, S. Jobic, P. Deniard and A. Demourgues, *Inorg. Chem.*, 2011, **50**, 2878–2884.
10 H. Serier-Brault, L. Thibault, M. Legrain, P. Deniard, X. Rocquefelte, P. Leone, J.-L. Perillon, S. Le Bris, J. Waku and S. Jobic, *Inorg. Chem.*, 2014, **53**, 12378–12383.
11 H. Liu, L. Yuan, S. Wang, H. Fang, Y. Zhang, C. Hou and S. Feng, *J. Mater. Chem. C*, 2016, **4**, 10529–10537.
12 Y. Yamasaki, Y. Kohara and Y. Tokura, *Phys. Rev. B: Condens. Matter Mater. Phys.*, 2009, **80**, 140412(R).
13 R. C. Lecraw, E. G. Spencer and C. S. Porter, *Phys. Rev.*, 1958, **110**, 1311–1313.
14 M. A. Gilleo and S. Geller, *Phys. Rev.*, 1958, **110**, 73–78.
15 S. Geller, *J. Appl. Phys.*, 1960, **31**, S30–S37.
16 R. Pauthenet, *J. Appl. Phys.*, 1959, **30**, S290–S292.
17 M. Deb, E. Popova, A. Fouchet and N. Keller, *Phys. Rev. B: Condens. Matter Mater. Phys.*, 2013, **87**, 224408.
18 L. Guo, K. Huang, Y. Chen, G. Li, L. Yuan, W. Peng, H. Yuan and S. Feng, *J. Solid State Chem.*, 2011, **184**, 1048–1053.
19 V. J. Fratello, C. D. Brandle, S. E. G. Slusky, A. J. Valentino, M. P. Norelli and R. Wolfe, *J. Cryst. Growth*, 1986, **75**, 281–283.
20 T.-J. Park, G. C. Papaefthymiou, A. J. Viescas, A. R. Moodenbaugh and S. S. Wong, *Nano Lett.*, 2007, **7**, 766–772.
21 S. Q. Yin, T. Sauyet, M. S. Seehra and M. Jain, *J. Appl. Phys.*, 2017, **121**, 063902.
22 T. Chen, Y. W. Zhang and W. L. Xu, *Phys. Chem. Chem. Phys.*, 2016, **18**, 22494–22502.
23 X. Rozanska, R. Fortrie and J. Sauer, *J. Am. Chem. Soc.*, 2014, **136**, 7751–7761.
24 X. C. Zhou, W. L. Xu, G. K. Liu, D. Panda and P. Chen, *J. Am. Chem. Soc.*, 2010, **132**, 138–146.
25 J. Grottrup, V. Postica, N. Ababii, O. Lupan, C. Zamponi, D. Meyners, Y. K. Mishra, V. Sontea, I. Tiginyanu and R. Adelung, *J. Alloys Compd.*, 2017, **701**, 920–925.
26 C. C. Yang and Y.-W. Mai, *Chem. Phys. Lett.*, 2012, **535**, 91–93.
27 N. Venkatram, R. Sathyavathi and D. Narayana Rao, *Opt. Express*, 2007, **15**, 12258–12263.
28 R. Viter, A. Katoch and S. S. Kim, *Met. Mater. Int.*, 2014, **20**, 163–167.
29 Y. Gupta, P. Arun, A. A. Naudi, M. V. Walz and E. A. Albanesi, *Thin Solid Films*, 2016, **612**, 310–316.
30 H. Tamaki, H. Watanabe, S. Kamiyama, Y. Oaki and H. Imai, *Angew. Chem., Int. Ed.*, 2014, **53**, 10706–10709.
31 H. Liu, L. Yuan, H. Qi, S. Wang, Y. Du, Y. Zhang, C. Hou and S. Feng, *Dyes Pigm.*, 2017, **145**, 418–426.
32 I. Ahmada, T. Abbas, A. B. Ziya, G. Abbas and A. Maqsood, *Mater. Res. Bull.*, 2014, **52**, 11–14.
33 W. J. Duan, S. H. Lu, Z. L. Wu and Y. S. Wang, *J. Phys. Chem. C*, 2012, **116**, 26043–26051.
34 A. Kumar and D. P. Ojha, *Indian J. Phys.*, 2016, **90**, 1041–1047.
35 P. B. A. Fechine, E. N. Silva, A. S. de Menezes, J. Derov, J. W. Stewart, A. J. Drehman, I. F. Vasconcelos, A. P. Ayala, L. P. Cardoso and A. S. B. Sombra, *J. Phys. Chem. Solids*, 2009, **70**, 202–209.
36 I. V. Chernyshova, M. F. Hochella Jr and A. S. Madden, *Phys. Chem. Chem. Phys.*, 2007, **9**, 1736–1750.
37 K. Z. Zheng, W. Y. Song, C. J. Lv, Z. Y. Liu and W. P. Qin, *CrystEngComm*, 2014, **16**, 4329–4337.
38 J. P. Hurrell, S. P. S. Porto, I. F. Chang, S. S. Mitra and R. P. Bauman, *Phys. Rev.*, 1968, **173**, 851–856.
39 L. Guo, H. Yuan, K. Huang, L. Yuan, S. Liu and S. Feng, *Chem. Res. Chin. Univ.*, 2011, **27**, 715–719.
40 M. Mullet, Y. Guillemin and C. Ruby, *J. Solid State Chem.*, 2008, **181**, 81–89.
41 C. Suchomski, C. Reitz, C. T. Sousa, J. P. Araujo and T. Brezesinski, *Chem. Mater.*, 2013, **25**, 2527–2537.
42 H. Qi, H. Liu, S. Wang, L. Yuan and C. Hou, *Chem. J. Chin. Univ.*, 2017, **38**, 535–540.
43 M.-S. Jang, I.-J. Roh, J. Park, C.-Y. Kang, W. J. Choi, S.-H. Baek, S. S. Park, J.-W. Yoo and K.-S. Lee, *J. Alloys Compd.*, 2017, **711**, 693–697.

